High-Order Shock-Capturing Methods for Study of Shock-Induced Turbulent Mixing with Adaptive Mesh Refinement Simulations

Man Long Wong
Sanjiva K. Lele

Advanced Modeling & Simulation Seminar

Jun 6th, 2019

Motivation

- **Richtmyer-Meshkov (RM) instability**, or **RMI**, occurs when a shock wave passes through a perturbed interface separating two fluids with different densities
- In natural phenomena/engineering applications:
  - Supernova explosion (SNe)
  - Inertial confinement fusion (ICF)
  - Supersonic combustion in scramjet

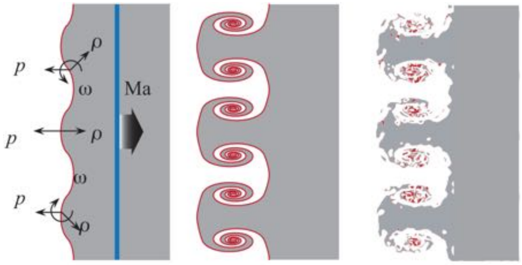

RMI evolution (Image Credit: B. M. Wilson, R. Mejia-Alvarez and K. P. Prestridge)

Supernova remnant (Image Credit: NASA/ESA/HEIC and The Hubble Heritage Team (STScI/AURA))

Motivation

- A lack of understanding of turbulent mixing induced from RMI, due to:
  - Only simultaneous measurements of density and velocity fields in 2D [1] [2]
  - Direct numerical simulations still too expensive
  - Methods to save computational cost:
    - High-order shock-capturing schemes
    - Adaptive gridding for localized and mobile features (shocks, mixing regions, etc.)
- High-order numerical schemes with adaptive mesh refinement (AMR) still not very popular for RMI simulations:
  - Tritschler et al.[3] used high-order schemes with uniform grid to study RMI with re-shock
  - Grinstein and Gowardhan[4] used AMR but only second order scheme for RMI simulations
  - Mcfarland et al.[5] also used second order scheme with AMR for inclined interface RMI

[1] Mohammad Mohaghar et al. "Evaluation of turbulent mixing transition in a shock-driven variable-density flow". In: *Journal of Fluid Mechanics* 831 (2017), pp. 779–825.

[2] Daniel T Reese et al. "Simultaneous direct measurements of concentration and velocity in the Richtmyer–Meshkov instability". In: *Journal of Fluid Mechanics* 849 (2018), pp. 541–575.

[3] VK Tritschler et al. "On the Richtmyer–Meshkov instability evolving from a deterministic multimode planar interface". In: *Journal of Fluid Mechanics* 755 (2014), pp. 429–462.

[4] FF Grinstein, AA Gowardhan, and AJ Wachtor. "Simulations of Richtmyer–Meshkov instabilities in planar shock-tube experiments". In: *Physics of Fluids* 23.3 (2011), p. 034106.

[5] Jacob A McFarland, Jeffrey A Greenough, and Devesh Ranjan. "Computational parametric study of a Richtmyer-Meshkov instability for an inclined interface". In: *Physical Review E* 84.2 (2011), p. 026303.

Motivation

- Goals of research:
  - Numerical framework for simulations of RMI and similar types of flows. The framework combines:
    - Improved high-order shock-capturing methods to preserve fine-scales better
    - AMR technique that only applies fine grid cells around localized features
  - Study the turbulent mixing induced by RMI through simulations:
    - Variable-density mixing effects
    - Effects of Reynolds number
    - Analyze the performance of reduced-order modeling through second-moment closures

Outline

1. A localized dissipation nonlinear scheme for shock- and interface-capturing in compressible flows
2. An adaptive mesh refinement framework for multi-species simulations with shock-capturing capability
3. High-resolution Navier-Stokes simulations of Richtmyer-Meshkov instability with re-shock
4. Budget of turbulent mass flux and its closure for Richtmyer-Meshkov instability

Weighted compact nonlinear schemes (WCNS's): governing equation

- Consider a scalar conservation law for 1D problem:

$$\frac{\partial u}{\partial t} + \frac{\partial f(u)}{\partial x} = 0$$

- Semi-discretize this equation on a grid with N points:

$$\frac{\partial u_j}{\partial t} + \left.\frac{\partial f(u)}{\partial x}\right|_j = 0$$

- Need a discrete approximation of the flux derivative:

$$\left.\frac{\partial f(u)}{\partial x}\right|_j$$

Illustration of methodology of WCNS's [6] [7]

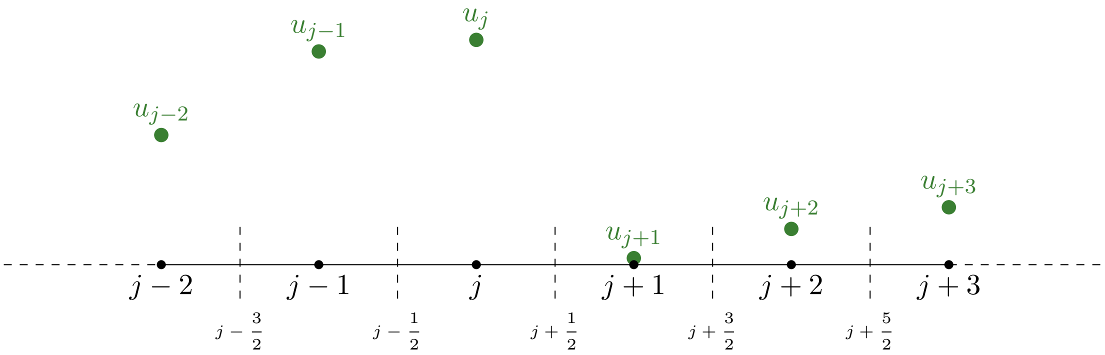

Given the solution values at cell nodes

[6] Xiaogang Deng and Hanxin Zhang. "Developing high-order weighted compact nonlinear schemes". In: *Journal of Computational Physics* 165.1 (2000), pp. 22–44.

[7] Shuhai Zhang, Shufen Jiang, and Chi-Wang Shu. "Development of nonlinear weighted compact schemes with increasingly higher order accuracy". In: *Journal of Computational Physics* 227.15 (2008), pp. 7294–7321.

Illustration of methodology of WCNS's [6] [7]

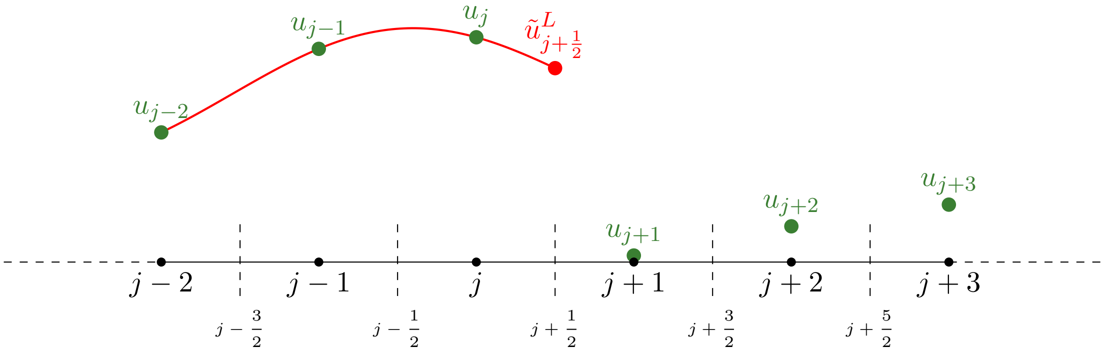

Left-biased interpolation for solution value at cell midpoint $\tilde{u}^L_{j+\frac{1}{2}}$

[6] Deng and Zhang, "Developing high-order weighted compact nonlinear schemes".

[7] Zhang, Jiang, and Shu, "Development of nonlinear weighted compact schemes with increasingly higher order accuracy".

Illustration of methodology of WCNS's [6] [7]

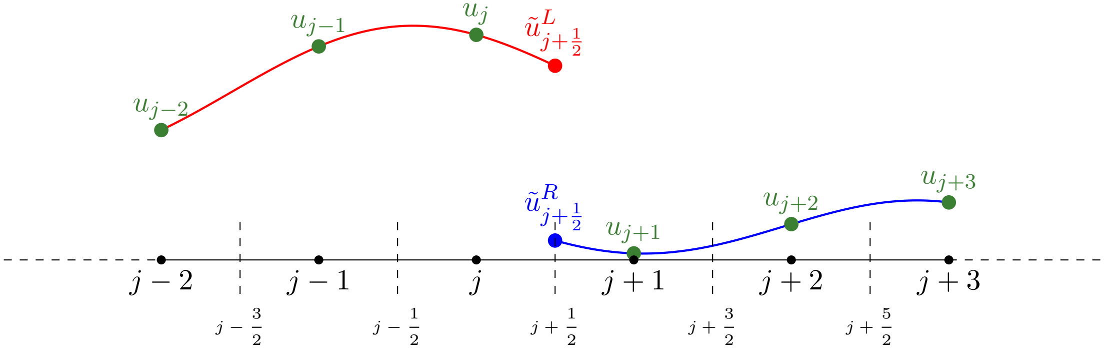

Right-biased interpolation for solution value at cell midpoint $\tilde{u}^R_{j+\frac{1}{2}}$

[6] Deng and Zhang, "Developing high-order weighted compact nonlinear schemes".

[7] Zhang, Jiang, and Shu, "Development of nonlinear weighted compact schemes with increasingly higher order accuracy".

Illustration of methodology of WCNS's [6] [7]

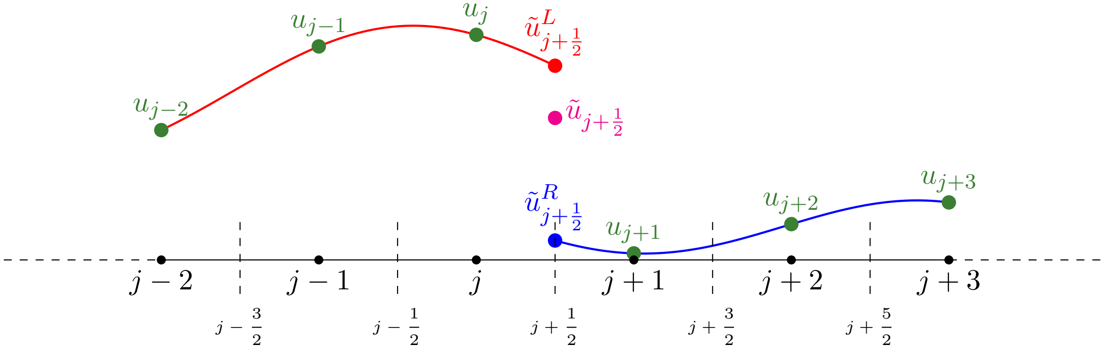

Flux-difference splitting method to get the interface solution value and flux at midpoint from left-biased and right-biased interpolated values

[6] Deng and Zhang, "Developing high-order weighted compact nonlinear schemes".

[7] Zhang, Jiang, and Shu, "Development of nonlinear weighted compact schemes with increasingly higher order accuracy".

Illustration of methodology of WCNS's [6] [7]

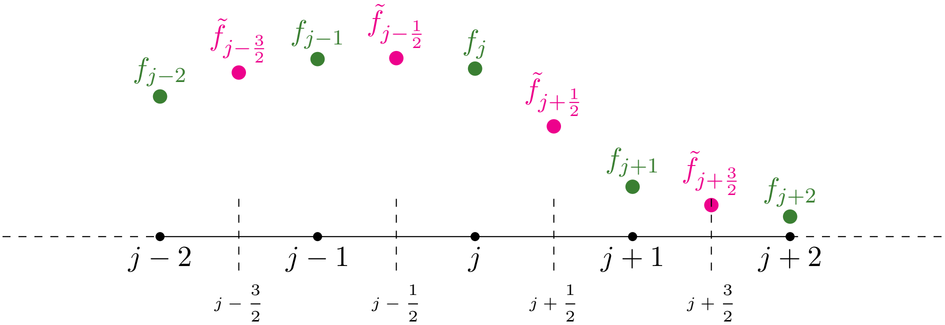

Explicit/compact finite difference to approximate $\left.\frac{\partial f(u)}{\partial x}\right|_j$ at nodes, e.g. explicit sixth order midpoint-and-node-to-node finite difference (MND):

$$\left.\frac{\partial f(u)}{\partial x}\right|_j \approx \frac{1}{\Delta x}\left[\frac{3}{2}\left(\tilde{f}_{j+\frac{1}{2}} - \tilde{f}_{j-\frac{1}{2}}\right) - \frac{3}{10}\left(f_{j+1} - f_{j-1}\right) - \frac{25}{384}\left(\tilde{f}_{j+\frac{3}{2}} - \tilde{f}_{j-\frac{3}{2}}\right)\right]$$

Left-biased explicit interpolations

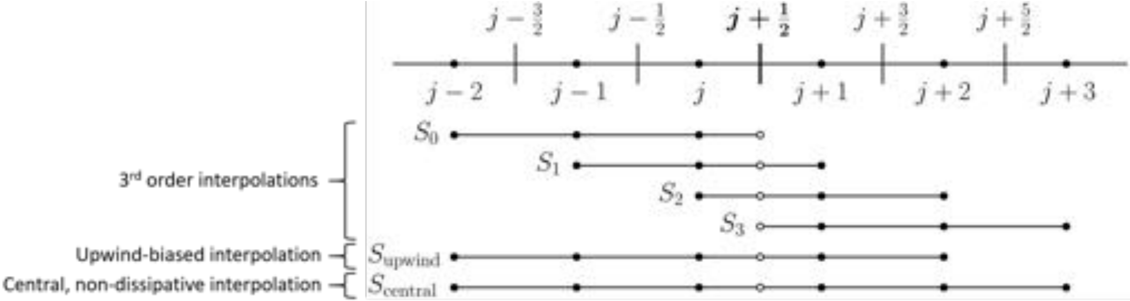

$$EI_0: \quad \tilde{u}^{(0)}_{j+\frac{1}{2}} = \frac{1}{8}\left(3u_{j-2} - 10u_{j-1} + 15u_j\right)$$

$$EI_1: \quad \tilde{u}^{(1)}_{j+\frac{1}{2}} = \frac{1}{8}\left(-u_{j-1} + 6u_j + 3u_{j+1}\right)$$

$$EI_2: \quad \tilde{u}^{(2)}_{j+\frac{1}{2}} = \frac{1}{8}\left(3u_j + 6u_{j+1} - u_{j+2}\right)$$

$$EI_3: \quad \tilde{u}^{(3)}_{j+\frac{1}{2}} = \frac{1}{8}\left(15u_{j+1} - 10u_{j+2} + 3u_{j+3}\right)$$

$$EI_{\text{upwind}} = \sum^{2} d_k^{\text{upwind}} EI_k \;\; (5^{\text{th}}\text{order}); \qquad EI_{\text{central}} = \sum^{3} d_k^{\text{central}} EI_k \;\; (6^{\text{th}}\text{order})$$

Nonlinear interpolations

In weighted essentially non-oscillatory (WENO) interpolations, the linear weights d_k are replaced with nonlinear weights ω_k for shock-capturing:

$$EI_{\text{upwind}} = \sum_{k=0}^{2} d_k^{\text{upwind}} EI_k \ \ (5^{\text{th}}\text{order}); \qquad EI_{\text{central}} = \sum_{k=0}^{3} d_k^{\text{central}} EI_k \ \ (6^{\text{th}}\text{order})$$

$$\downarrow$$

$$EI_{\text{nonlinear}} = \sum_{k=0}^{2} \omega_k^{\text{upwind}} EI_k \quad / \quad \sum_{k=0}^{3} \omega_k^{\text{central}} EI_k$$

- ω_k^{upwind}: traditional WENO weights by Jiang and Shu (JS)[8] and improved weights (Z)[9]
- $\omega_k^{\text{central}}$: CU-M2 weights [10]

[8] Guang-Shan Jiang and Chi-Wang Shu. "Efficient implementation of weighted ENO schemes". In: *Journal of computational physics* 126.1 (1996), pp. 202–228.

[9] Rafael Borges et al. "An improved weighted essentially non-oscillatory scheme for hyperbolic conservation laws". In: *Journal of Computational Physics* 227.6 (2008), pp. 3191–3211.

[10] XY Hu and Nikolaus A Adams. "Scale separation for implicit large eddy simulation". In: *Journal of Computational Physics* 230.19 (2011), pp. 7240–7249.

Locally dissipative (LD) nonlinear weights

- The LD[11] nonlinear weights (**hybrid weights**) are introduced for localized dissipation at shocks or discontinuities for regularization:

$$\omega_k = \begin{cases} \sigma\ \omega_k^{\mathrm{upwind}} + (1-\sigma)\ \omega_k^{\mathrm{central}}, & \text{if } R_\tau > \alpha_{RL}^{\tau} \\ \omega_k^{\mathrm{central}}, & \text{otherwise} \end{cases}, \quad k = 0, 1, 2, 3$$

  where R_τ is a relative smoothness indicator. σ is a shock sensor.
- Ensure minimal numerical dissipation in smooth regions (central interpolation) and one-sided interpolation at discontinuities
- $\omega_k^{\mathrm{upwind}}$ is the Z nonlinear weights and $\omega_k^{\mathrm{central}}$ is **improved** from CU-M2 nonlinear weights for localized numerical dissipation

[11] Man Long Wong and Sanjiva K Lele. "High-order localized dissipation weighted compact nonlinear scheme for shock-and interface-capturing in compressible flows". In: *Journal of Computational Physics* 339 (2017), pp. 179–209.

Approximate dispersion relation (ADR) technique[12]

- For linear schemes, analytical dispersion and dissipation characteristics can be obtained from Fourier analysis
- ADR used to compute the characteristics of the nonlinear schemes numerically:

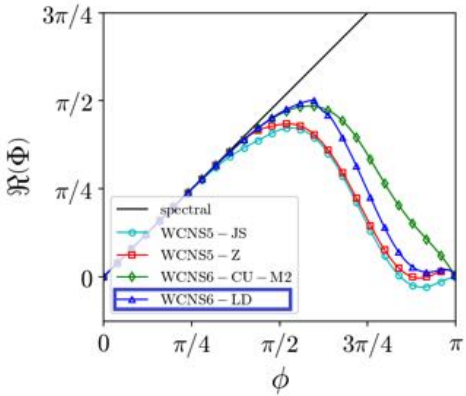

(a) Dispersion characteristics

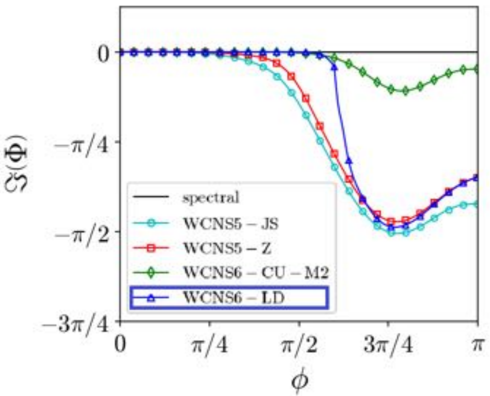

(b) Dissipation characteristics

[12] Sergio Pirozzoli. "On the spectral properties of shock-capturing schemes". In: *Journal of Computational Physics* 219.2 (2006), pp. 489–497.

Numerical tests: 1D shock tube problems

1. Shu-Osher problem[13] [200 points]: Mach 3 shock interacting with a sinusoidal density field

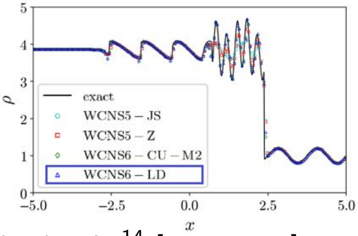

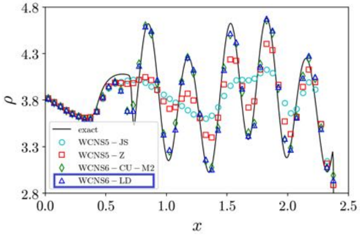

2. Multi-species shock tube[14] [100 points]:

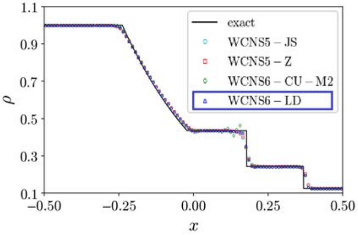

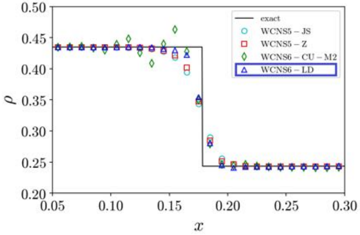

[13] Chi-Wang Shu and Stanley Osher. "Efficient implementation of essentially non-oscillatory shock-capturing schemes". In: *Journal of Computational Physics* 77.2 (1988), pp. 439–471.

Numerical test: 2D double Mach reflection[15]

- A Mach 10 shock impinges on the wall, and a complex shock reflection structure evolves
- Kelvin-Helmholtz instability along the slip line is only damped by numerical dissipation
- The smaller the numerical dissipation, the more the rolled up vortices along the slip line

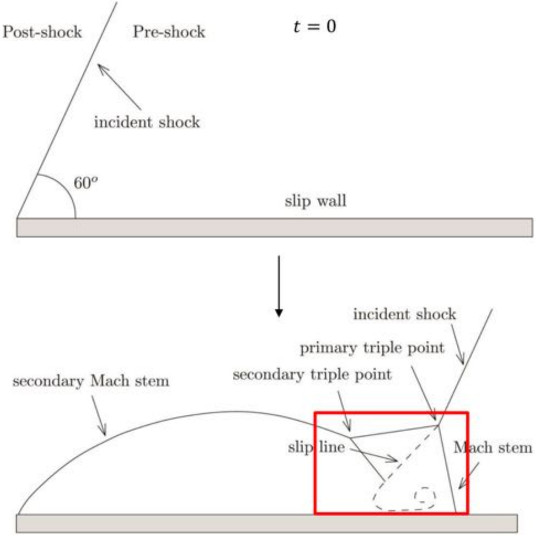

[15] Phillip Colella and Paul R Woodward. "The piecewise parabolic method (PPM) for gas-dynamical simulations". In: *Journal of computational physics* 54.1 (1984), pp. 174–201.

Numerical test: 2D double Mach reflection (cont.)

- Density contours [Full domain grid size: 960×240]:

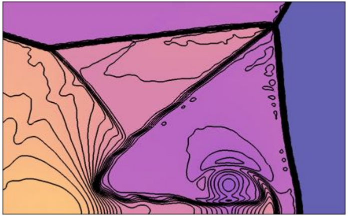

(a) WCNS5-JS

(b) WCNS5-Z

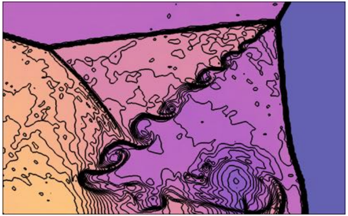

(c) WCNS6-CU-M2

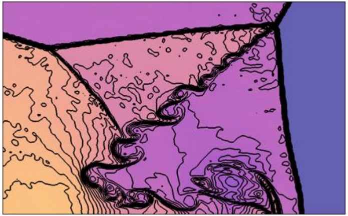

(d) $\boxed{\mathrm{WCNS6-LD}}$

- WCNS5-JS and WCNS5-Z too dissipative to produce rolled-up vortices along the slip line
- WCNS6-CU-M2 and WCNS6-LD can capture much more fine-scale vortical structures along the slip line

Numerical test: 3D Taylor-Green vortex

- An essentially incompressible periodic problem
- As time evolves, the inviscid vortex stretches and produces features at smaller scales
- Zero Q-criterion at $t = 8$ with 64^3 grid:

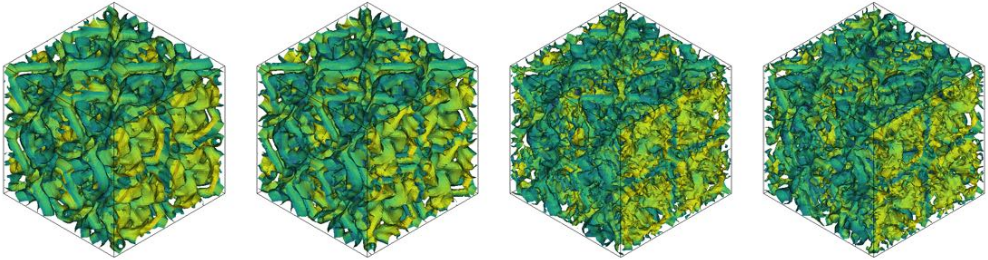

(a) WCNS5-JS (b) WCNS5-Z (c) WCNS6-CU-M2 (d) $\boxed{\mathrm{WCNS6-LD}}$

- Finer features are captured with WCNS6-CU-M2 and WCNS6-LD

Numerical test: 3D Taylor-Green vortex (cont.)

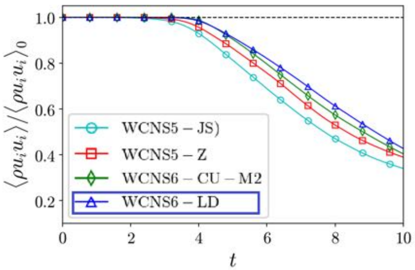

(a) Kinetic energy

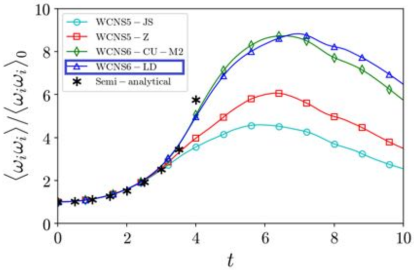

(b) Enstrophy

Spectra of u at $t = 5$:

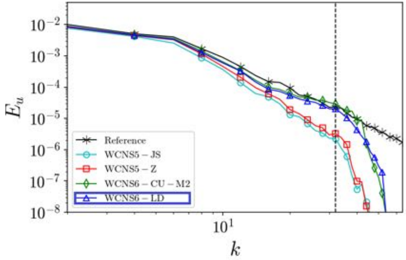

- WCNS6-LD preserves more KE over times
- Both WCNS6's outperform WCNS5's in predicting growth of enstrophy
- Both WCNS6's can better capture features up to high wavenumber

Summary

- Improved nonlinear interpolation developed for a type of nonlinear schemes for problems with shocks and material interfaces
- The interpolation adaptively switches between one-sided interpolation around discontinuities and non-dissipative central interpolation in smooth regions
- The improved scheme WCNS-LD:
  - robust at shocks and discontinuities through the regularization
  - good resolution and low dissipation properties that are more suited for vortical features

Outline

Overview of patch-based adaptive mesh refinement (AMR)

- Patch-based AMR[16][17] designed for uniform structured Cartesian grids
- A hierarchy of nested "patches" of levels of varying grid resolution
- **Multi-time stepping** with Runge-Kutta schemes:

$$\frac{\Delta t_l}{\Delta x_l} = \frac{\Delta t_{l-1}}{\Delta x_{l-1}} = \cdots = \frac{\Delta t_0}{\Delta x_0}$$

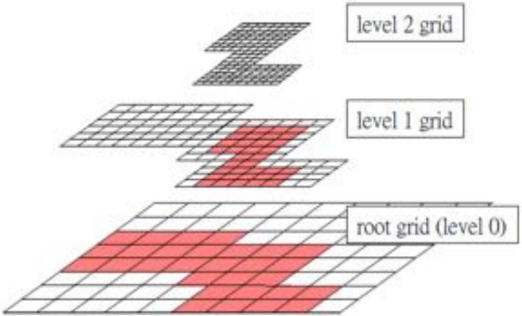

- Requires numerical scheme in **conservative** form for treatment at coarse-fine AMR grid boundaries to ensure **discrete conservation**:

$$\frac{\partial u_{i,j}}{\partial t} + \frac{\widehat{F}_{i+\frac{1}{2},j} - \widehat{F}_{i-\frac{1}{2},j}}{\Delta x} + \frac{\widehat{G}_{i,j+\frac{1}{2}} - \widehat{G}_{i,j-\frac{1}{2}}}{\Delta y} = 0$$

[16] Marsha J Berger and Phillip Colella. "Local adaptive mesh refinement for shock hydrodynamics". In: *Journal of computational Physics* 82.1 (1989), pp. 64–84.

[17] Marsha J Berger and Joseph Oliger. "Adaptive mesh refinement for hyperbolic partial differential equations". In: *Journal of computational Physics* 53.3 (1984), pp. 484–512.

Relation between finite difference schemes and flux difference form[18]

- For a central finite difference scheme (compact or explicit) for flux derivative:

$$\alpha \widehat{F}'_{j-1} + \beta \widehat{F}'_{j} + \alpha \widehat{F}'_{j+1} = \frac{1}{\Delta x}\Big(-a_{\frac{5}{2}} F_{j-2} - a_2 F_{j-\frac{3}{2}} - a_{\frac{3}{2}} F_{j-1} - a_1 F_{j-\frac{1}{2}} + a_1 F_{j+\frac{1}{2}} + a_{\frac{3}{2}} F_{j+1} + a_2 F_{j+\frac{3}{2}} + a_{\frac{5}{2}} F_{j+2}\Big)$$

- Can be rewritten into flux difference form:

$$\alpha \widehat{F}_{j-\frac{1}{2}} + \beta \widehat{F}_{j+\frac{1}{2}} + \alpha \widehat{F}_{j+\frac{3}{2}} = a_{\frac{5}{2}} F_{j-1} + a_2 F_{j-\frac{1}{2}} + \left(a_{\frac{3}{2}} + a_{\frac{5}{2}}\right) F_j + \left(a_1 + a_2\right) F_{j+\frac{1}{2}} + \left(a_{\frac{3}{2}} + a_{\frac{5}{2}}\right) F_{j+1} + a_2 F_{j+\frac{3}{2}} + a_{\frac{5}{2}} F_{j+2}$$

s.t.

$$\boxed{\widehat{F}'_j = \frac{1}{\Delta x}\left(\widehat{F}_{j+\frac{1}{2}} - \widehat{F}_{j-\frac{1}{2}}\right)}$$

[18] A Subramaniam, ML Wong, and SK Lele. "A High-Order Weighted Compact High Resolution Scheme with Boundary Closures for Compressible Turbulent Flows with Shocks". In: *arXiv preprint arXiv:1809.05784* (2018).

Hydrodynamics Adaptive Mesh Refinement Simulator (HAMeRS)[19]

In-house flow solver built on parallel SAMRAI library from LLNL to simulate compressible single-species and multi-species flows with adaptive mesh refinement (AMR) and high-order shock-capturing methods:

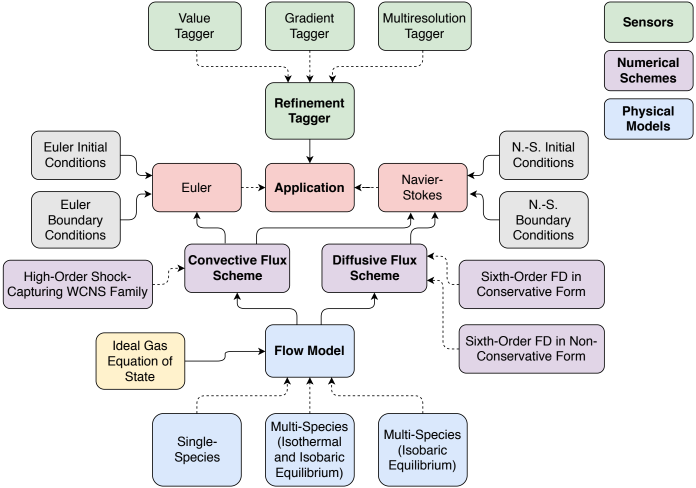

[19] Man Long Wong. *Hydrodynamics Adaptive Mesh Refinement Simulator*. https://github.com/mlwong/HAMeRS. 2018.

Numerical test: 2D inviscid shock-vortex interaction[20]

- Isentropic vortex interacts with Mach 1.2 stationary shock
- Distorted vortex produces reflected shocks
- Multiple sound waves generated from reflected shock-vortex interaction

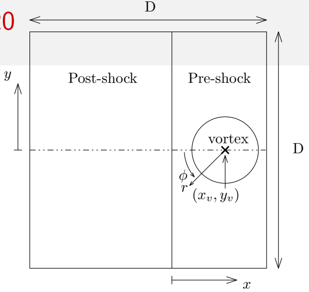

Sound pressure, $(p - p_\infty) / \left(\rho_\infty c_\infty^2\right)$, of reference solution with grid resolution 4096×4096:

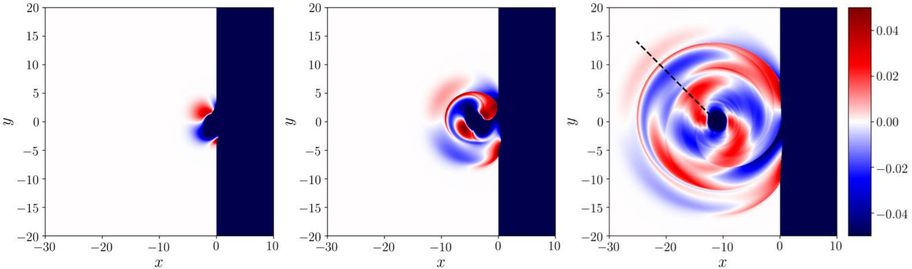

(a) $t = 4$ (b) $t = 8$ (c) $t = 16$

[20] Osamu Inoue and Yuji Hattori. "Sound generation by shock–vortex interactions". In: *Journal of Fluid Mechanics* 380 (1999), pp. 81–116.

Numerical test: 2D inviscid shock-vortex interaction (cont.)

Refined regions of AMR simulation with base grid resolution 128×128 and $1:2$ refinement ratio (green: level 1; red: level 2):

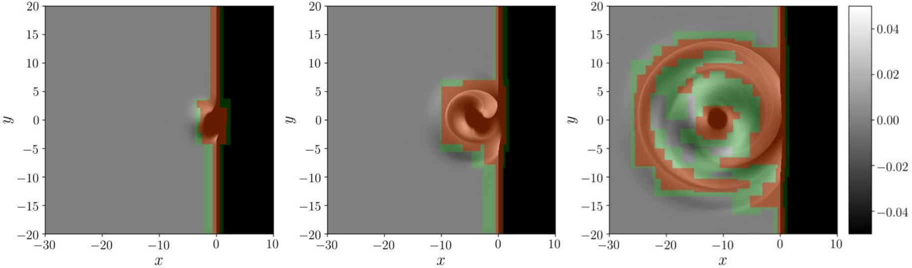

(a) $t = 4$ (b) $t = 8$ (c) $t = 16$

Comparison with 512×512 uniform grid simulation:

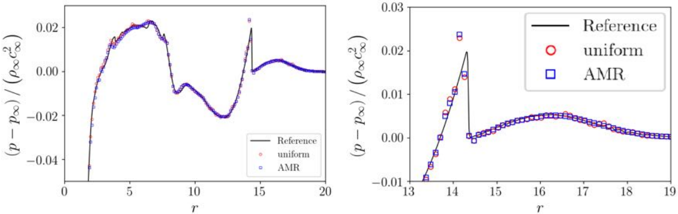

(a) Global sound pressure (b) Local sound pressure

Numerical test: 2D inviscid shock-vortex interaction (cont.)

- Weighted number of cells:

$$\sum_{l=0}^{l_{max}} \omega_l N_l, \quad \omega_l = \frac{\Delta x_{l_{max}}}{\Delta x_l}$$

- In this test problem:

$$\omega_0 = 1/4,$$
$$\omega_1 = 1/2,$$
$$\omega_2 = 1$$

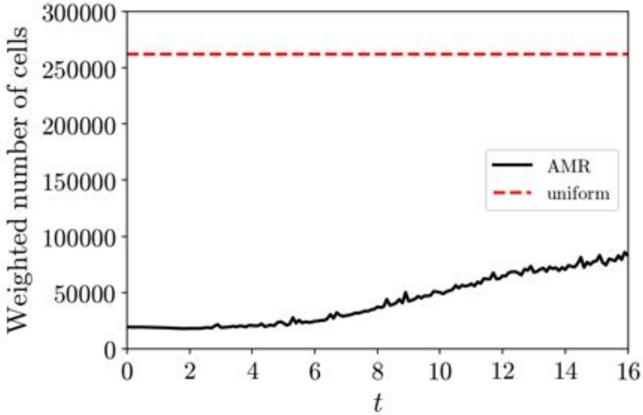

Weighted number of cells of AMR simulation $\approx$ 30% of number of cells of uniform grid (262144 cells) simulation at the end

Numerical test: 3D viscous shock-bubble interaction

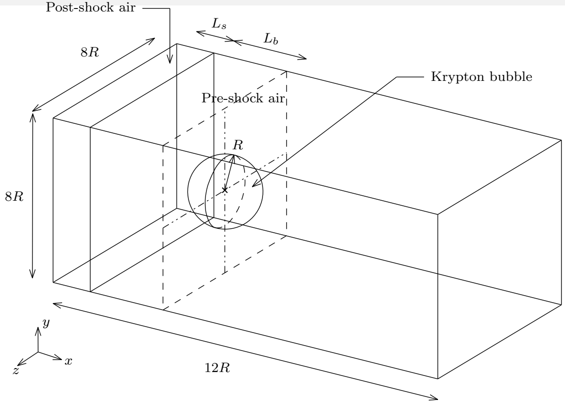

- $Ma_s = 1.68$, $R = 1.016$ mm
- Material interface with characteristic length scale $\epsilon_i = 0.125$ mm
- A quadrant of the domain is simulated
- Different grids settings:

Grid	Base grid resolution	Refinement ratios	Finest grid spacing (μm)
A	$384 \times 128 \times 128$	1:2, 1:2	7.94
B	$768 \times 256 \times 256$	1:2, 1:2	3.97
C	$1536 \times 512 \times 512$	1:2, 1:2	1.98

- Gradient sensor on pressure, multiresolution sensor on density, and sensor on mass fraction used for refinement

Numerical test: 3D viscous shock-bubble interaction (cont.)

- Conservative multi-component Navier-Stokes equations for ideal fluid mixture are solved:

$$\frac{\partial \rho Y_i}{\partial t} + \nabla \cdot (\rho \boldsymbol{u} Y_i) + \nabla \cdot \boldsymbol{J_i} = 0$$
$$\frac{\partial \rho \boldsymbol{u}}{\partial t} + \nabla \cdot (\rho \boldsymbol{u}\boldsymbol{u} + p\boldsymbol{\delta} - \boldsymbol{\tau}) = 0$$
$$\frac{\partial E}{\partial t} + \nabla \cdot [(E+p)\, \boldsymbol{u}] - \nabla \cdot (\boldsymbol{\tau} \cdot \boldsymbol{u} - \boldsymbol{q_c} - \boldsymbol{q_d}) = 0$$

  where ρ, $\boldsymbol{u}$, p and E are the density, velocity vector, pressure and total energy of the fluid mixture respectively. Y_i is the mass fraction of species $i = 1, 2, ..., N$, with N the total number of species.

- $\boldsymbol{J_i}$ is diffusive mass flux for each species. $\boldsymbol{\tau}$, $\boldsymbol{q_c}$ and $\boldsymbol{q_d}$ are viscous stress tensor, conductive heat flux and inter-species diffusional enthalpy flux respectively of the mixture.
- Sixth order finite differences for viscous and diffusive fluxes

Numerical test: 3D viscous shock-bubble interaction (cont.)

- Density fields in xy plane at $z = 0$ of AMR simulation with grid C:

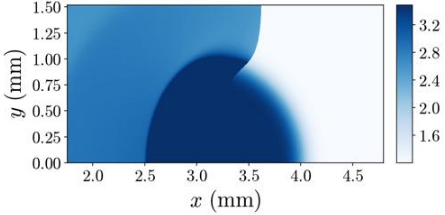

(a) $t = 2.8$ μs

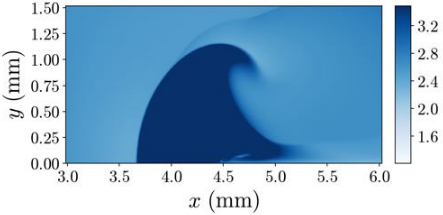

(b) $t = 8.8$ μs

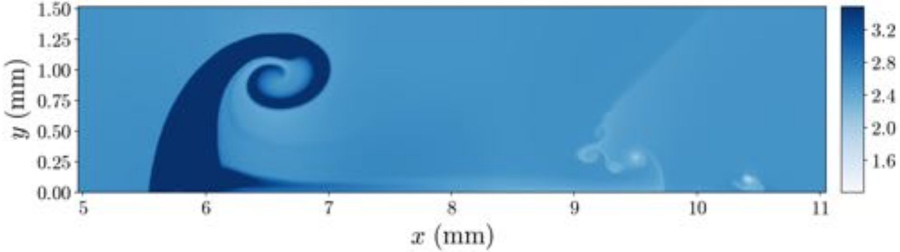

(c) $t = 17.6$ μs

Numerical test: 3D viscous shock-bubble interaction (cont.)

- Refined regions (green: level 1; red: level 2):

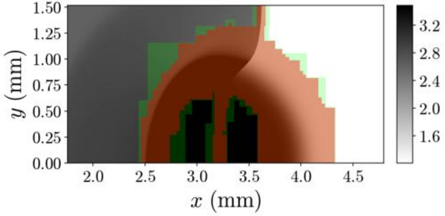

(a) $t = 2.8\ \mu$s

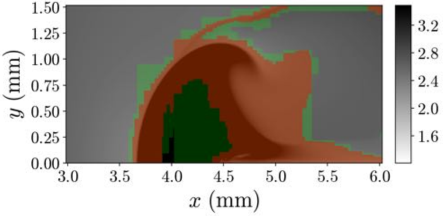

(b) $t = 8.8\ \mu$s

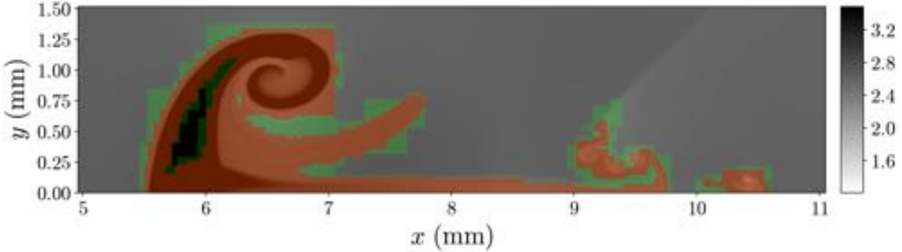

(c) $t = 17.6\ \mu$s

Numerical test: 3D viscous shock-bubble interaction (cont.)

3D visualization of mass fraction with grid C at end of simulation $t = 17.6\ \mu s$

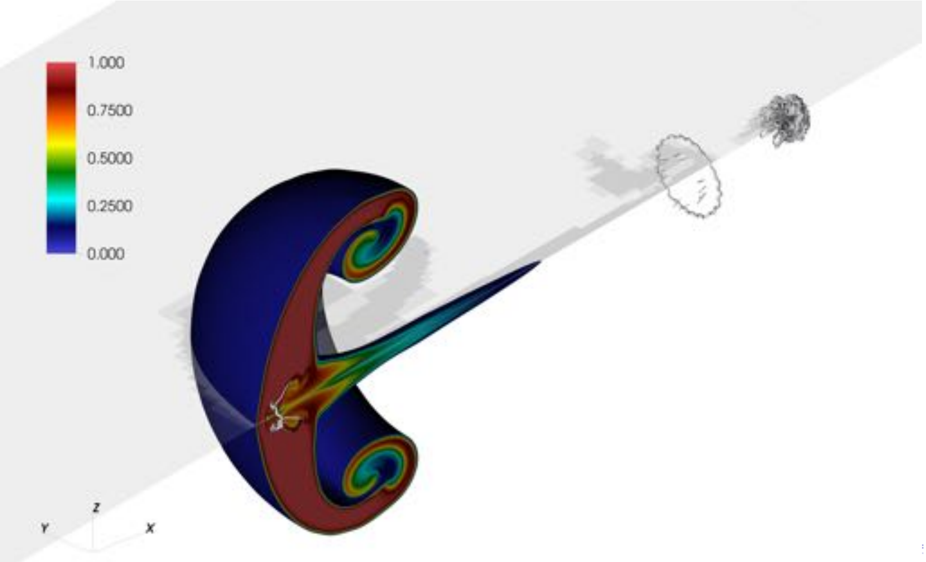

Numerical test: 3D viscous shock-bubble interaction (cont.)

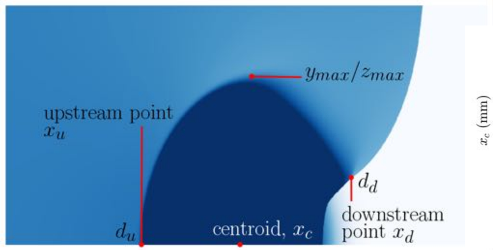

- y_{max} is y coordinate of the upper point with $\mathrm{SF_6}$ concentration equals $0.01\max(\mathrm{Y_{SF6}})$

$$l_x = x_d - x_u$$

$$l_{yz} = y_{max} + z_{max}$$

- All statistical quantities of interests are grid converged

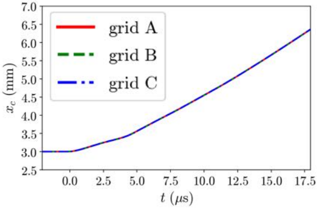

(a) Centroid

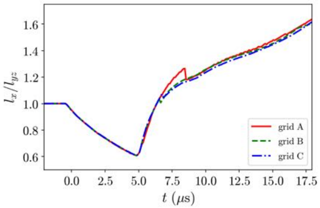

(b) l_x/l_y

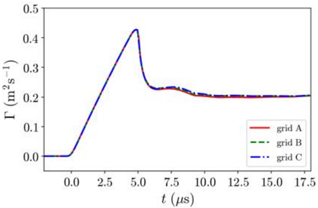

(c) Circulation

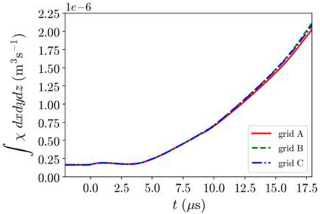

(d) Integrated scalar dissipation rate

Summary

- AMR framework developed for multi-species CFD applications
- Physics-based sensors such as gradient and multiresolution sensors implemented to detect features for refinement
- Framework successfully tested with simulations[21] that consist of interactions between shocks, material interfaces, and vortices
- The sensors for mesh refinement can successfully identify:
    - Shock wave and acoustic waves
    - Vortical feautes
    - Mixing regions

[21] One more 2D viscous shock-cylinder interaction problem is presented in thesis

Outline

Problem setup

- Compressible 2D and 3D multi-species Navier-Stokes simulations set up to study shock-induced mixing between SF_6 and air due to RM instability:

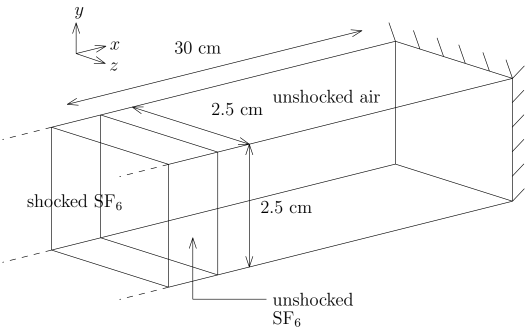

(a) 3D configuration

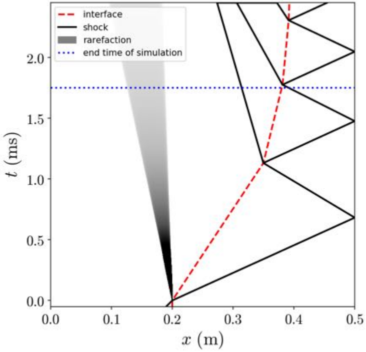

(b) Space-time (x-t) diagram

- $Ma_s = 1.45$
- $At = \dfrac{\rho_{\mathrm{SF}_6} - \rho_{\mathrm{air}}}{\rho_{\mathrm{SF}_6} + \rho_{\mathrm{air}}} = 0.68$
- 2D domain is cross-section of the 3D domain
- Mixing region shocked **twice** (first shock and re-shock)

Perturbations

Perturbation modes seeded on the interfaces:

- 2D: $$S(y) = A \sum_m \cos\left(\frac{2\pi m}{L_y} y + \phi_m\right)$$
- 3D: $$S(y,z) = A \sum_m \cos\left(\frac{2\pi m}{L_{yz}} y + \phi_m\right) \cos\left(\frac{2\pi m}{L_{yz}} z + \psi_m\right)$$
- 11 modes in total: $0.833 \text{ mm} \le \lambda_m \le 1.25 \text{ mm}$
- $A = 0.0141 \text{ mm}$

- Estimated with impulsive theory, 2D and 3D problems have same:
  - linear growth rates $\dot{\eta}_{imp}$
  - time scales τ_c

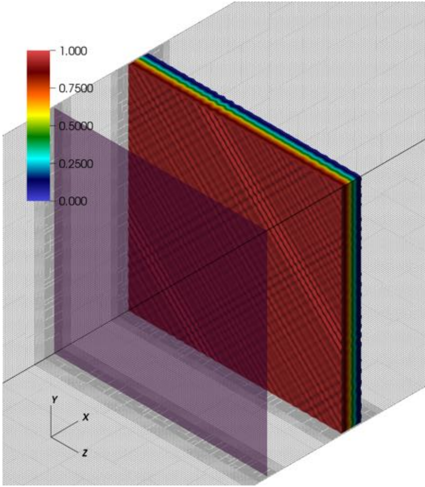

initial conditions

Configurations of 2D and 3D adaptive mesh refinement (AMR) simulations

- Simulated with the AMR solver (HAMeRS)
- Sixth order WCNS-LD for convective flux
- Sixth order finite differences for diffusive and viscous fluxes
- Three levels of adaptive meshes (two levels of AMR)
- Gradient and multiresolution sensors; also sensor on mass fraction field
- Grid resolutions used for convergence test:

2D Grid	Base Grid Resolution	Refinement Ratio	Finest Grid Spacing (mm)
D	2560×128	1:2, 1:4	0.0244
E	5120×256	1:2, 1:4	0.0122
F	10240×512	1:2, 1:4	0.0061
G	20480×1024	1:2, 1:4	0.0031

3D Grid	Base Grid Resolution	Refinement Ratio	Finest Grid Spacing (mm)	Maximum Weighted Number of Cells
B	$640 \times 32 \times 32$	1:2, 1:4	0.0977	30M
C	$1280 \times 64 \times 64$	1:2, 1:4	0.0488	144M
D	$2560 \times 128 \times 128$	1:2, 1:4	0.0244	778M

- $\sim$34 points across smallest initial wavelength for grid D

Visualizations of mole fraction (3D, grid D)

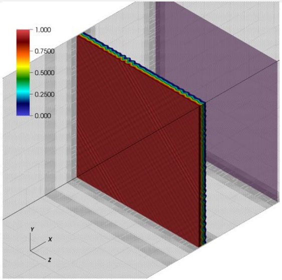

(a) $t = 0.05$ ms (after first shock)

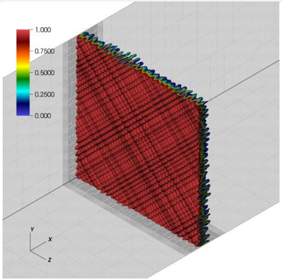

(b) $t = 0.40$ ms

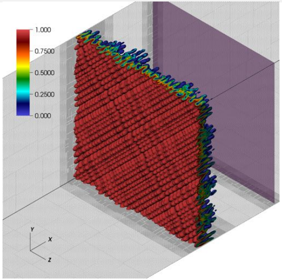

(c) $t = 1.10$ ms (before re-shock)

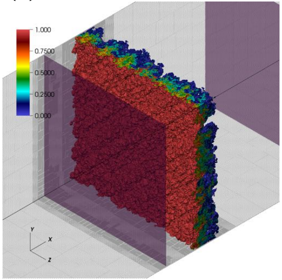

(d) $t = 1.20$ ms (after re-shock)

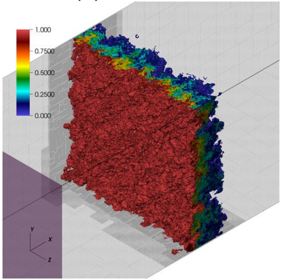

(e) $t = 1.40$ ms

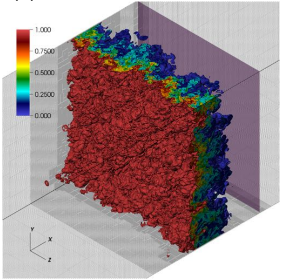

(f) $t = 1.75$ ms

2D grid convergence study (over 24 realizations)

Mixing width $W = \int 4\bar{X}_{\mathrm{SF}_6}(1-\bar{X}_{\mathrm{SF}_6})dx$; Mixedness $\Theta = \dfrac{\int \overline{X_{SF_6}(1-X_{SF_6})}dx}{\int \bar{X}_{\mathrm{SF}_6}(1-\bar{X}_{\mathrm{SF}_6})dx}$; $\mathrm{TKE} = \dfrac{1}{2}\rho u_i'' u_i''$

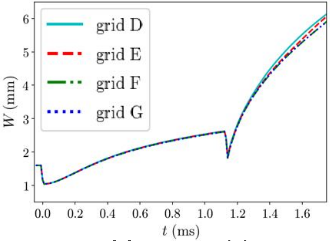

(a) Mixing width

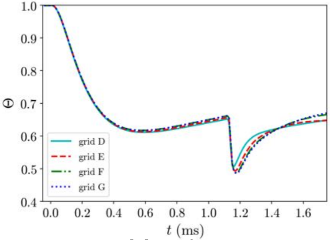

(b) Mixedness

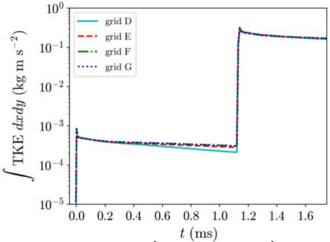

(c) TKE (integrated)

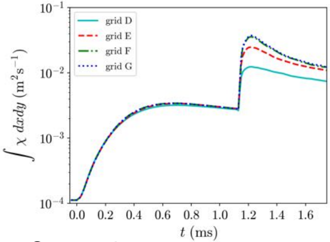

(d) Scalar dissipation rate (integrated)

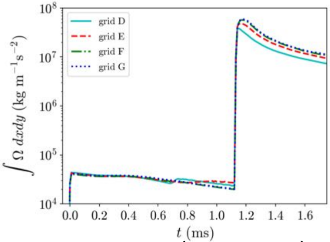

(e) Enstrophy (integrated)

3D grid convergence study

Mixing width $W = \int 4\bar{X}_{\mathrm{SF}_6}(1-\bar{X}_{\mathrm{SF}_6})dx$; Mixedness $\Theta = \dfrac{\int \overline{X_{SF_6}(1-X_{SF_6})}dx}{\int \bar{X}_{\mathrm{SF}_6}(1-\bar{X}_{\mathrm{SF}_6})dx}$; $\mathrm{TKE} = \frac{1}{2}\rho u_i'' u_i''$

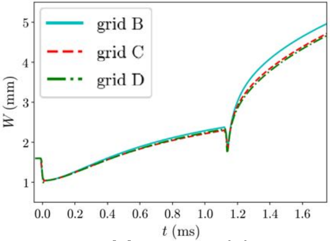

(a) Mixing width

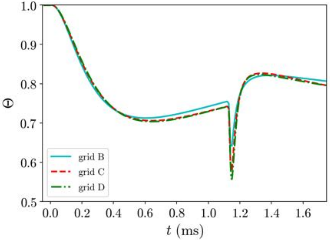

(b) Mixedness

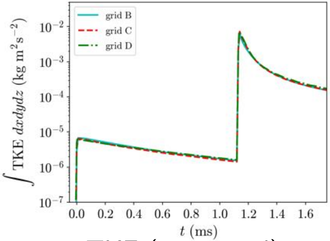

(c) TKE (integrated)

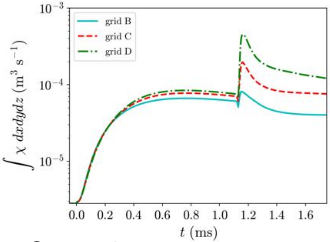

(d) Scalar dissipation rate (integrated)

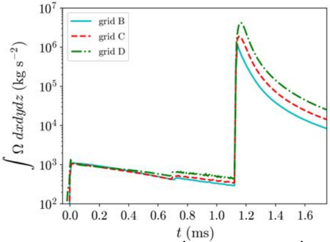

(e) Enstrophy (integrated)

Mole fraction fields $t^* = t/\tau_c$

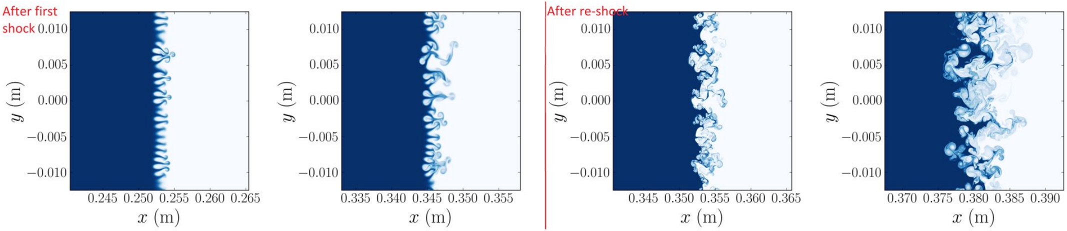

(a) $t^* = 7.5$ $(t = 0.40 \text{ ms})$ (b) $t^* = 20.7$ $(t = 1.10 \text{ ms})$ (c) $t^* = 22.6$ $(t = 1.20 \text{ ms})$ (d) $t^* = 32.9$ $(t = 1.75 \text{ ms})$

2D, grid G

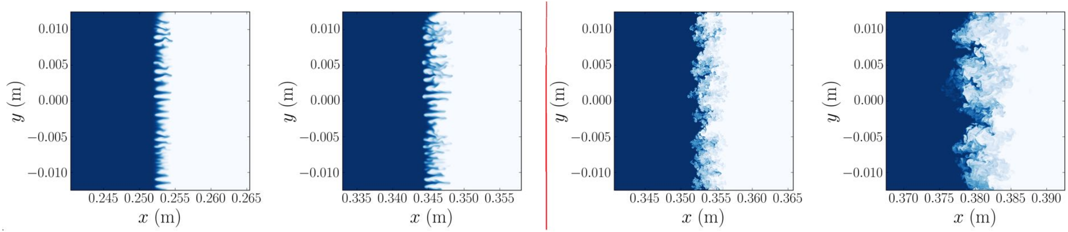

(a) $t^* = 7.5$ $(t = 0.40 \text{ ms})$ (b) $t^* = 20.7$ $(t = 1.10 \text{ ms})$ (c) $t^* = 22.6$ $(t = 1.20 \text{ ms})$ (d) $t^* = 32.9$ $(t = 1.75 \text{ ms})$

3D, grid D

Reduced Reynolds number 3D simulations

- Reynolds number Re_W is reduced by increasing physical transport coefficients (TC's) by factors of 2 & 4 (μ, μ_v, D, and κ). This is as same as cases with reduced Re_W, while Sc and Pr unchanged.

$$Re_W = \frac{\bar{\rho} u_{rms} W}{\bar{\mu}}, \quad \text{where } u_{rms} = \sqrt{\overline{u_i'' u_i''}/3}$$

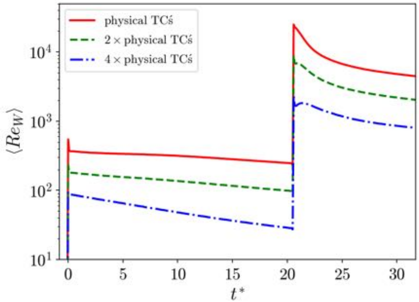

- $\langle \cdot \rangle$ is additional averaging in central part of mixing layer: $4\bar{X}_{\mathrm{SF_6}}(1 - \bar{X}_{\mathrm{SF_6}}) > 0.9$

Mole fraction fields

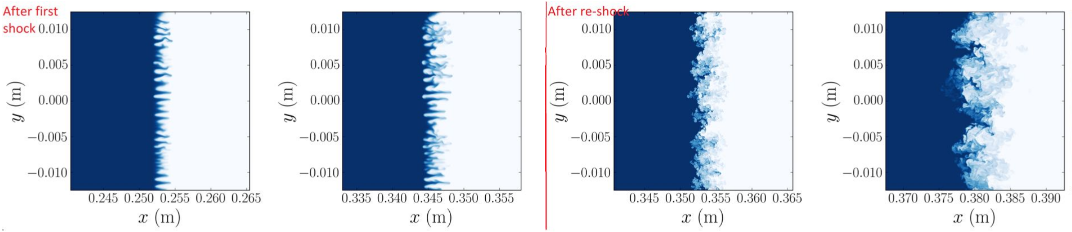

(a) $t^* = 7.5 \ (t = 0.40 \text{ ms})$ (b) $t^* = 20.7 \ (t = 1.10 \text{ ms})$ (c) $t^* = 22.6 \ (t = 1.20 \text{ ms})$ (d) $t^* = 32.9 \ (t = 1.75 \text{ ms})$

Physical transport coefficients, grid D

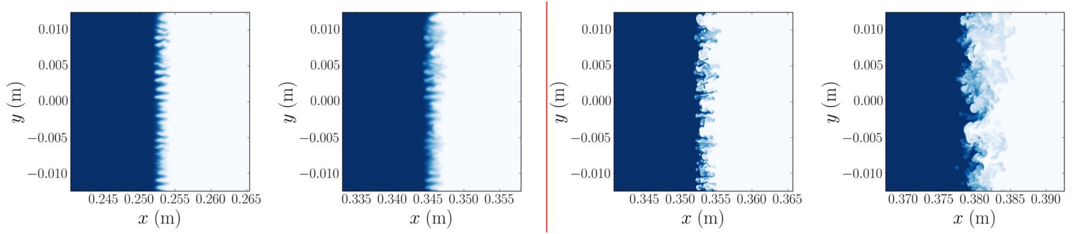

(a) $t^* = 7.5 \ (t = 0.40 \text{ ms})$ (b) $t^* = 20.7 \ (t = 1.10 \text{ ms})$ (c) $t^* = 22.6 \ (t = 1.20 \text{ ms})$ (d) $t^* = 32.9 \ (t = 1.75 \text{ ms})$

$4\times$ physical transport coefficients, grid D

Flow compressibility and effective Atwood number

- Turbulent Mach number Ma_t and effective Atwood number At_e:

$$Ma_t = \frac{\sqrt{3}u_{rms}}{\bar{c}}, \quad At_e = \frac{\sqrt{\overline{\rho'^2}}}{\bar{\rho}}$$

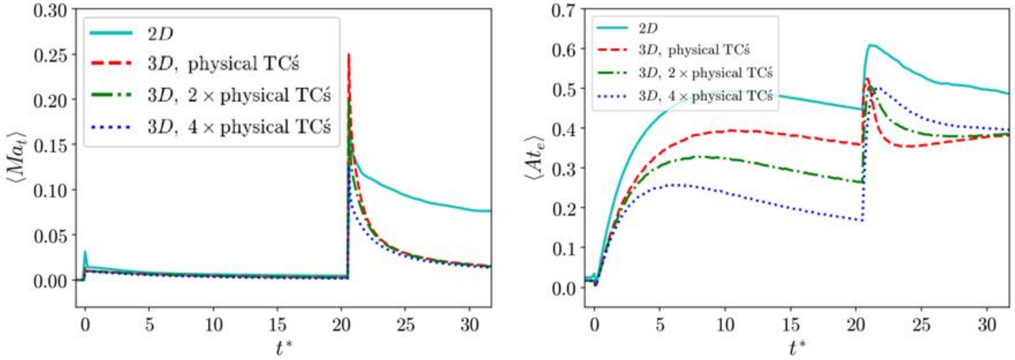

- Flows are weakly compressible
- $At_e \approx 0$ due to initially diffuse interface, but flows become non-Boussinesq ($At_e > 0.05$) as the interfaces become sharper after first shock and re-shock

Mixing: mixing width

- The mixing width is normalized by $\dot{\eta}_{imp}$ and τ_c: $W^* = \dfrac{W - W|_{t=0}}{\dot{\eta}_{imp}\tau_c}$

- With physical TC's, W^* of 2D case grows at a faster rate compared to that of 3D case after first shock initially but growth rates are similar at late times
- After re-shock, the 2D mixing width grows at a much faster rate
- 3D case with reduced Reynolds number has slower growth rate in mixing width before re-shock but growth rates are similar after re-shock

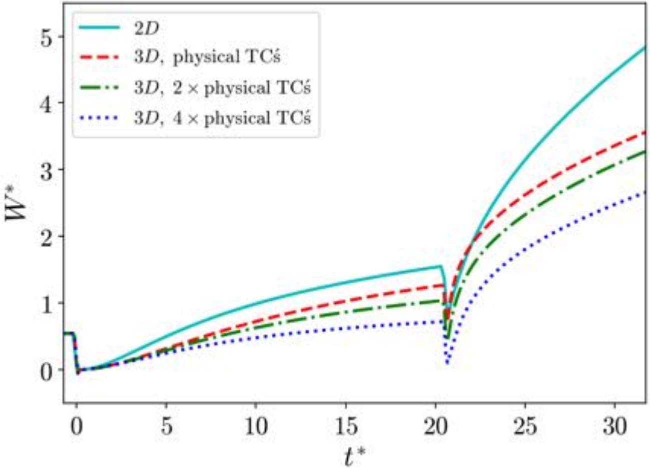

Mixing: mixedness

- The mixedness is defined as:

$$\Theta = \frac{\int \overline{X_{SF_6}(1 - X_{SF_6})} dx}{\int \bar{X}_{SF_6}\left(1 - \bar{X}_{SF_6}\right) dx}$$

- Mixedness quantifies the amount of fluids molecularly mixed within the mixing region
- The 2D and 3D mixednes values are converging to 0.7 and 0.8 respectively [0.85 for 3D RMI from Tritschler et al.[22], 0.8 for 3D RMI from Mohaghar et al.[23]]

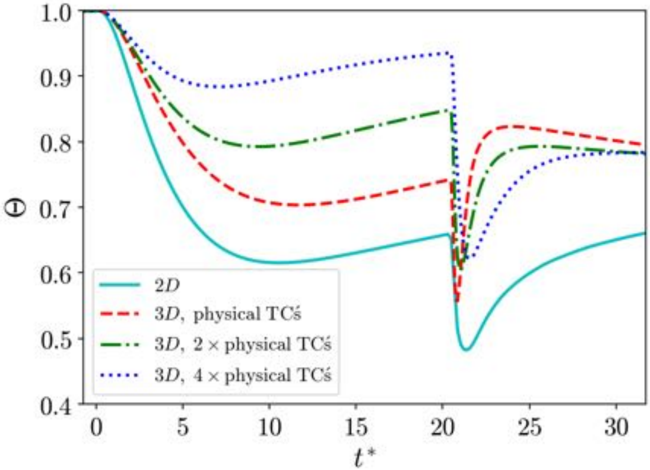

[22] Tritschler et al., "On the Richtmyer–Meshkov instability evolving from a deterministic multimode planar interface".

[23] Mohaghar et al., "Evaluation of turbulent mixing transition in a shock-driven variable-density flow".

Mixing: mole fraction profiles

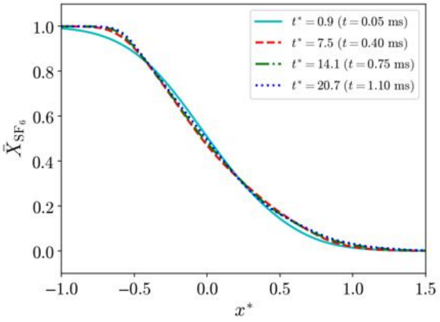

(a) After first shock, before reshock, 3D

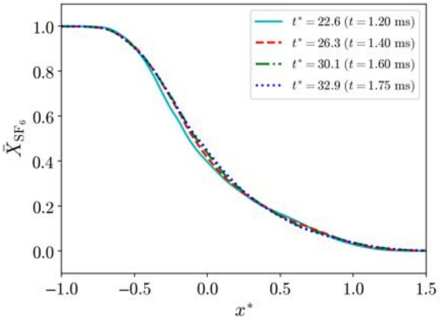

(b) After reshock, 3D

- The normalized position is defined as: $$x^* = \frac{x - x_i}{W(t)}$$
- Asymmetric, spikes penetrate more than bubbles
- Profiles collapse quite well at late times, similar to planar Rayleigh-Taylor instability[24]

[24] Daniel Livescu et al. "High-Reynolds number Rayleigh–Taylor turbulence". In: *Journal of Turbulence* 10 (2009), N13.

Mixing: mole fraction variance profiles

- $\Theta = \dfrac{\int \overline{X_{\mathrm{SF}_6}\left(1 - X_{\mathrm{SF}_6}\right)} dx}{\int \bar{X}_{\mathrm{SF}_6}\left(1 - \bar{X}_{\mathrm{SF}_6}\right) dx} = 1 - 4 \int \overline{X_{SF_6}'^2} dx^*$

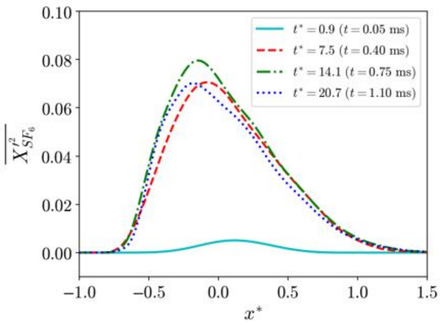

(a) After first shock, before reshock, 3D

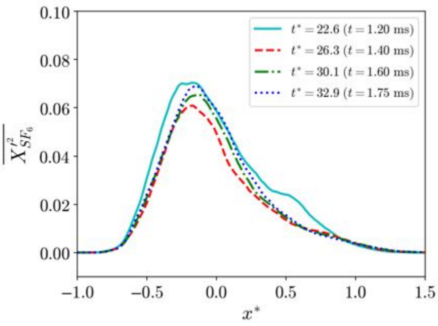

(b) After reshock, 3D

- Fluids harder to mix in the heavier fluid side indicated by larger variance
- Approaching self-similarity near end of simulations

TKE time evolution

- TKE is defined as:

$$\mathrm{TKE} = \frac{1}{2}\rho u_i'' u_i''$$

- TKE decays at faster rate for 3D problem compared to 2D
- Among 3D cases, TKE decays at faster rate before re-shock for case with smaller Reynolds number
- After re-shock, all 3D cases have similar TKE decay rates

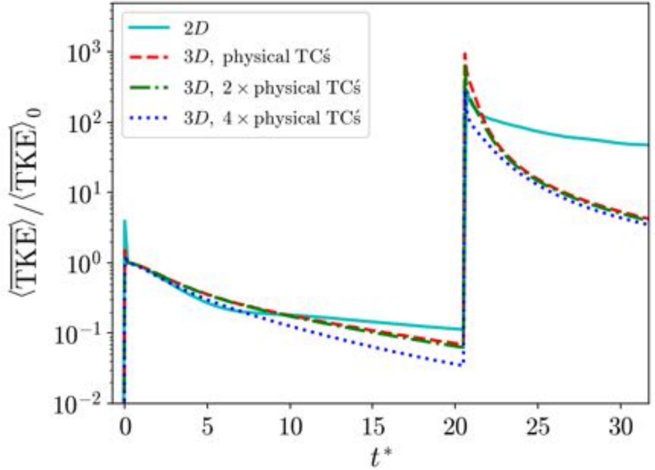

Turbulent kinetic energy (TKE) profiles

- The TKE is normalized as: $\mathrm{TKE}^* = \dfrac{(\mathrm{TKE})\, W}{\int \overline{\mathrm{TKE}}\, dx}$

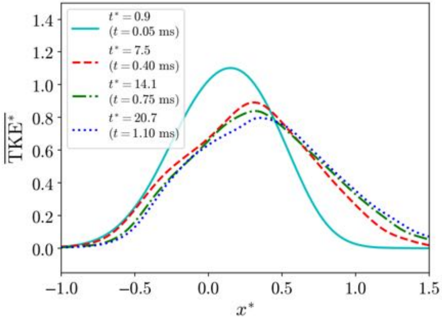

(a) After first shock, before reshock, 3D

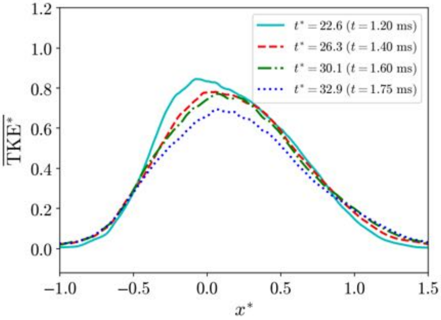

(b) After reshock, 3D

- Peak of TKE is biased towards the lighter fluid side, especially before re-shock

Anisotropy

- The Reynolds stress anisotropy tensor b_{ij} for 2D and 3D flows defined as:

$$b_{ij}^{2D} = \frac{\tilde{R}_{ij}}{\tilde{R}_{kk}} - \frac{1}{2}\delta_{ij}, \quad b_{ij}^{3D} = \frac{\tilde{R}_{ij}}{\tilde{R}_{kk}} - \frac{1}{3}\delta_{ij}, \quad \text{where } \tilde{R}_{ij} = \frac{\overline{\rho u_i'' u_j''}}{\bar{\rho}}$$

- 2D Reynolds normal stresses becoming isotropic at a faster rate than 3D stresses before re-shock
- After re-shock, 2D Reynolds normal stresses become isotropic

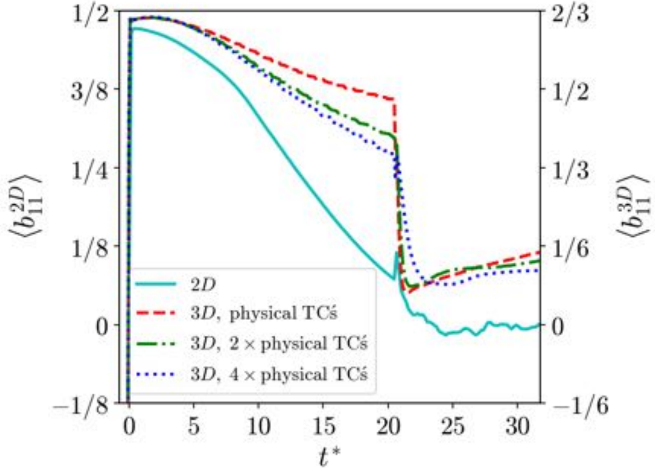

Summary

- 2D and 3D RMI have very different time evolution for mixing width and TKE and final mixedness values
- Reynolds stresses of 2D flow approaching isotropy quickly after both shocks; Reynolds stresses of 3D flows remain anisotropic at the of simulations
- Fluids are more difficult to mix in 2D configuration

- Reducing Re_W has significant effect before re-shock:
  - smaller growth rate of W
  - larger Θ
  - larger decay rate of TKE
- Reynolds number has much smaller effect on the growth of mixing width/decay of TKE after re-shock

More analysis on probability density functions and spectra can be found in manuscript submitted to Physical Review Fluids[25]

[25] Man Long Wong, Daniel Livescu, and Sanjiva K. Lele. "High-resolution Navier-Stokes simulations of Richtmyer-Meshkov instability with re-shock". In: *arXiv preprint arXiv:1812.01785* (2018).

Outline

1. A localized dissipation nonlinear scheme for shock- and interface-capturing in compressible flows

2. An adaptive mesh refinement framework for multi-species simulations with shock-capturing capability

3. High-resolution Navier-Stokes simulations of Richtmyer-Meshkov instability with re-shock

4. Budget of turbulent mass flux and its closure for Richtmyer-Meshkov instability

Favre-averaged momentum equation

- Direct numerical simulation (DNS) or large eddy simulation (LES) still very expensive
- Reynolds-averaged / Favre-averaged Navier-Stokes (RANS/FANS) simulation with **turbulence modeling** is an interim tool
- Most turbulent mixing models **only tested with experimental results** for RM turbulence
- **High-fidelity simulation data** also important for model validation
- Favre-averaged momentum equation ($\tilde{\cdot} = \overline{\rho(\cdot)}/\bar{\rho}$):

$$\frac{\partial \left(\bar{\rho}\tilde{u}_i\right)}{\partial t} + \frac{\partial \left(\bar{\rho}\tilde{u}_k\tilde{u}_i\right)}{\partial x_k} = -\frac{\partial \left(\bar{p}\delta_{ki}\right)}{\partial x_k} + \frac{\partial \bar{\tau}_{ki}}{\partial x_k} - \frac{\partial \left(\bar{\rho}\tilde{R}_{ki}\right)}{\partial x_k}$$

- $\tilde{R}_{ij} = \overline{\rho u_i'' u_j''}/\bar{\rho}$: Favre-averaged Reynolds stress

Reynolds stress

- Algebaric closure model based on turbulent kinetic energy is not good:

$$\tilde{R}_{ij} \approx \frac{2}{3}k\delta_{ij} - 2C_{\mu}S\sqrt{k}\tilde{S}_{ij}, \quad \tilde{S}_{ij} = \frac{1}{2}\left(\frac{\partial \tilde{u}_i}{\partial x_j} + \frac{\partial \tilde{u}_j}{\partial x_i}\right) - \frac{1}{3}\frac{\partial \tilde{u}_k}{\partial x_k}\delta_{ij},$$

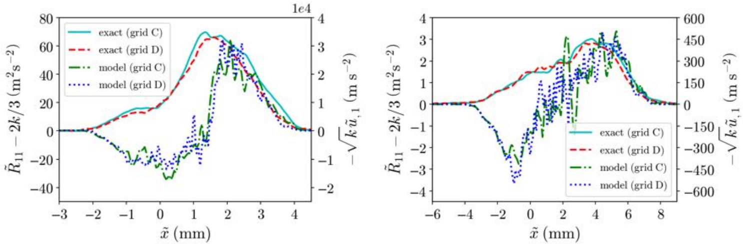

(a) $t = 1.20$ ms (b) $t = 1.75$ ms

- To improve, transport equation of $\tilde{R}_{ij}$ is considered:

$$\underbrace{\frac{\partial \bar{\rho}\tilde{R}_{ij}}{\partial t}}_{\text{ROC}} + \underbrace{\frac{\partial\left(\bar{\rho}\tilde{u}_k\tilde{R}_{ij}\right)}{\partial x_k}}_{\text{convection}} = \underbrace{a_i\left(\frac{\partial \bar{p}}{\partial x_j} - \frac{\bar{\tau}_{jk}}{\partial x_k}\right) + a_j\left(\frac{\partial \bar{p}}{\partial x_i} - \frac{\partial \bar{\tau}_{ik}}{\partial x_k}\right) - \bar{\rho}\tilde{R}_{ik}\frac{\partial \tilde{u}_j}{\partial x_k} - \bar{\rho}\tilde{R}_{jk}\frac{\partial \tilde{u}_i}{\partial x_k}}_{\text{production}}$$

+ turbulent transport (unclosed) + pressure strain redistribution (unclosed) + dissipation (unclosed)

Turbulent mass flux and density-specific-volume covariance

- $a_i = \overline{\rho' u_i'}/\bar{\rho}$: velocity associated with turbulent mass flux
- To close $\bar{\rho} a_i$, BHR model by Besnard et al.[26] suggests to model transport of $\bar{\rho} a_i$:

$$\underbrace{\frac{\partial \left(\bar{\rho} a_i\right)}{\partial t}}_{\text{ROC}} + \underbrace{\frac{\partial \left(\bar{\rho} \tilde{u}_k a_i\right)}{\partial x_k}}_{\text{convection}} = \underbrace{b \left(\frac{\partial \bar{p}}{\partial x_i} - \frac{\partial \bar{\tau}_{ki}}{\partial x_k} \right) - \tilde{R}_{ik} \frac{\partial \bar{\rho}}{\partial x_k}}_{\text{production}} + \text{redistribution}$$
$$+ \text{ turbulent transport (unclosed)} + \text{ destruction (unclosed)}$$

- $b = -\overline{\rho' (1/\rho)'}$: density-specific-volume covariance
- BHR-3 model by Schwarzkopf et al.[27] recommends to model transport of $\bar{\rho} b$:

$$\underbrace{\frac{\partial \bar{\rho} b}{\partial t}}_{\text{ROC}} + \underbrace{\frac{\partial \left(\bar{\rho} \tilde{u}_k b\right)}{\partial x_k}}_{\text{convection}} = \underbrace{-2 \left(b + 1\right) a_k \frac{\partial \bar{\rho}}{\partial x_k}}_{\text{production}} + \text{redistribution} + \text{ turbulent transport (unclosed)}$$
$$+ \text{ destruction (unclosed)}$$

[26] Didier Besnard et al. *Turbulence transport equations for variable-density turbulence and their relationship to two-field models.* Tech. rep. Los Alamos National Lab., NM (United States), 1992.

[27] John D Schwarzkopf et al. “Application of a second-moment closure model to mixing processes involving multicomponent miscible fluids”. In: *Journal of Turbulence* 12 (2011), N49.

Profiles of $\bar{\rho} a_1$ (in moving frame of interface)

- Using highest Reynolds number 3D case in previous section
- $\tilde{x} = x - x_i$, where x_i is location of interface
- After both first shock and re-shock, $\bar{\rho} a_1$ spreads and the peak decreases over time

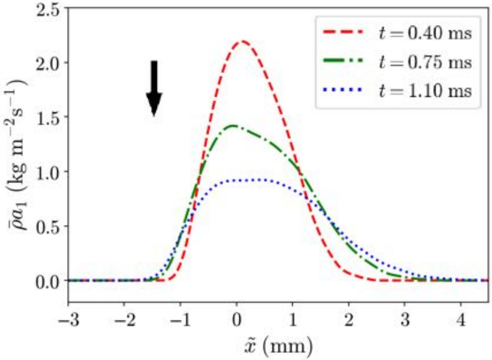

(a) After first shock, before re-shock

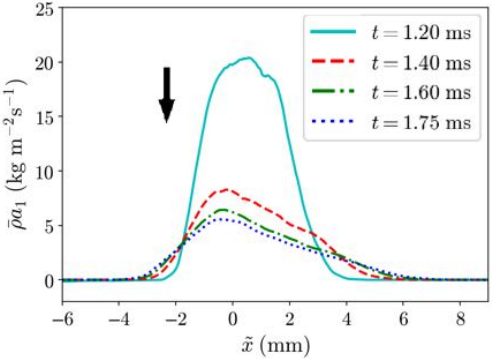

(b) After re-shock

Budget of turbulent mass flux, $\bar{\rho}a_1$ (in moving frame of interface)

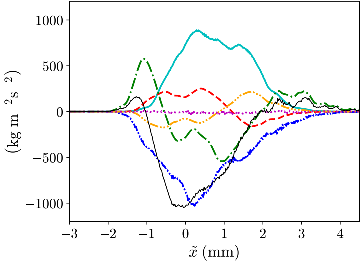

(a) $t = 1.10$ ms (before re-shock)

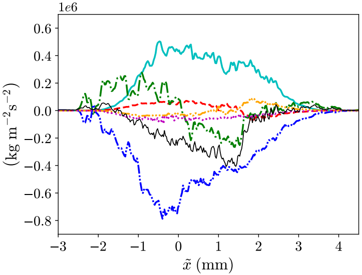

(b) $t = 1.20$ ms (after re-shock)

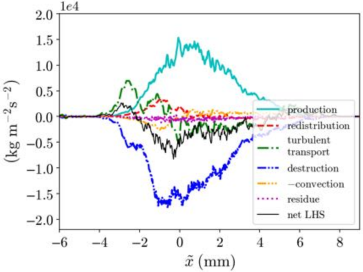

(c) $t = 1.75$ ms

- The production and destruction (unclosed) terms are dominant terms in the budget
- The net LHS (rate of change + convection) is negative in the middle part of mixing layer, causing $\bar{\rho}a_1$ to decrease in magnitude after first shock and re-shock
- Turbulent transport (unclosed) term spreads the profile
- Redistribution and convection terms are small over time

Budget of turbulent mass flux, $\bar{\rho}a_1$

- Destruction consists of three unclosed components: $\bar{\rho}\overline{(1/\rho)'p'_{,1}}$, $-\bar{\rho}\overline{(1/\rho)'\tau'_{1i,i}}$, $\bar{\rho}\epsilon_{a_1} = -\bar{\rho}\overline{u'_i\frac{\partial u'_k}{\partial x_k}}$
- $\bar{\rho}\overline{(1/\rho)'p'_{,1}}$ is the only important term after re-shock

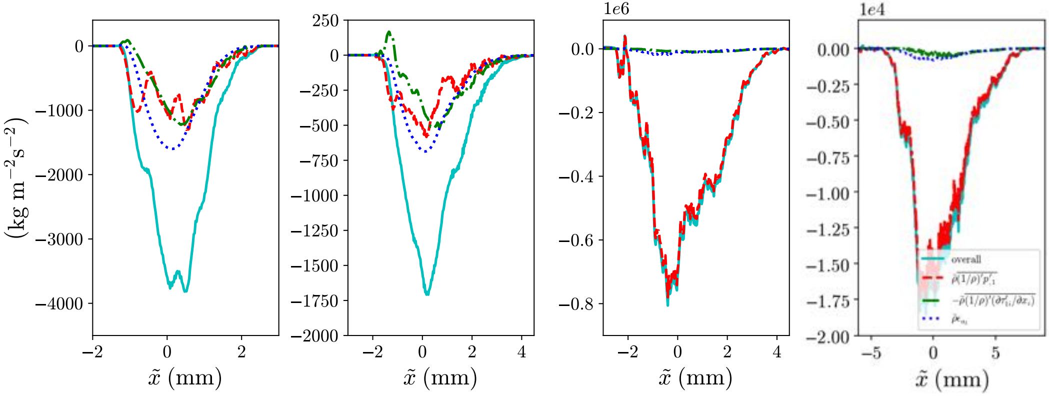

(a) $t = 0.40$ ms (b) $t = 1.10$ ms (before re-shock) (c) $t = 1.20$ ms (after re-shock) (d) $t = 1.75$ ms

Assessment of BHR-3[29] model: unclosed terms of transport equation of $\bar{\rho} a_1$

- Turbulent mass flux, $\bar{\rho} a_1$:

Unclosed Term	Exact Form	Modeled Form [28]
Turbulent transport	$-\bar{\rho}\dfrac{\partial\left(\overline{\rho' u' u'/\bar{\rho}}\right)}{\partial x}$	$2C_a\bar{\rho}\dfrac{\partial\left[\left(S\tilde{R}_{11}/\sqrt{k}\right)a_{1,1}\right]}{\partial x}$
Destruction	$\bar{\rho}\left(\dfrac{1}{\rho}\right)'\dfrac{\partial p'}{\partial x}$	$-C_{a1}\bar{\rho}\dfrac{\sqrt{k}}{S}a_1$

- C_a amd C_{a1} are model coefficients; S is a turbulent length scale
- Assuming S uniform inside mixing region (ignoring S), cancelling common terms and operators for analyzing validity of model **after re-shock** (after mixing transition has occurred)

[28] $k = \tilde{R}_{ii}/2$ is turbulent kinetic energy per unit mass

[29] Schwarzkopf et al., "Application of a second-moment closure model to mixing processes involving multicomponent miscible fluids".

BHR-3 assessment: unclosed terms of $\bar{\rho}a_1$ transport equation (after re-shock)

- Turbulent transport:

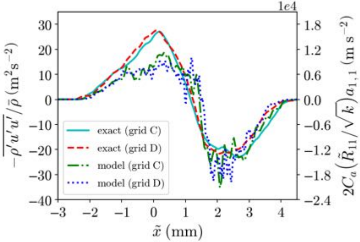

(a) $t = 1.20$ ms

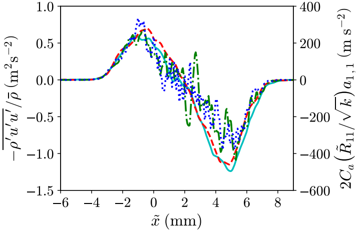

(b) $t = 1.75$ ms

- Destruction:

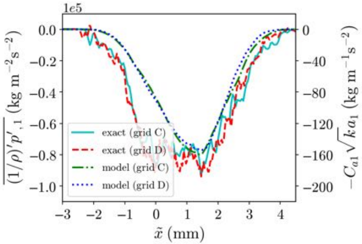

(a) $t = 1.20$ ms

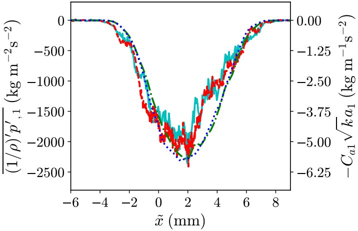

(b) $t = 1.75$ ms

BHR-3 assessment: turbulent length scales S (after re-shock)

- W: integral mixing width
- **Least square fit** within mixing region to estimate **S**'s **required** for turbulent transport and destruction terms of $\bar{\rho}a_1$
- Two length scale turbulence model BHR3.1 [Schwarzkopf et al., 2015] seems unnecessary for a_1

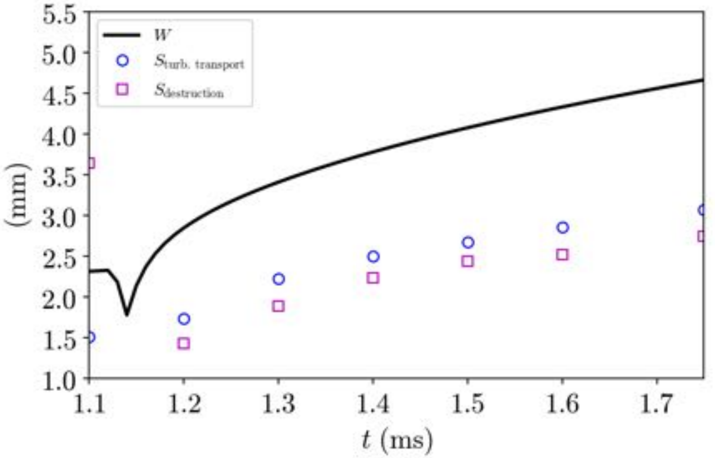

Summary

- $\bar{\rho}a_i$ plays an important role for modeling of $\tilde{R}_{ij}$ in BHR-3 model
- $\bar{\rho}a_1$ transport equation was analyzed
- Destruction term in budget of $\bar{\rho}a_1$ has different composition before and after re-shock (after mixing transition)
- BHR-3 model captures shapes of unclosed terms of $\bar{\rho}a_1$ transport equation well
- S's required for modeling unclosed terms of $\bar{\rho}a_1$ transport equation dependent on each other

Analysis of budgets and closures for $\tilde{R}_{ij}$ and b discussed in thesis

Conclusions

- High-resolution and localized dissipation schemes improved for shock problems that involve flow instabilities and turbulence
- AMR framework was developed and shown to be robust for problems that involve shocks and multi-species
- Asymmetric variable-density mixing effects examined
- Reynolds number has large effect on the flows before re-shock (before mixing transition)
- The BHR-3 model has good modeling assumptions for the $\bar{\rho}a_1$ transport equation for post-transition flows

Questions?

The PhD research was partially supported by Los Alamos National Laboratory, under grant number 431679.